Application of high-order vorticity confinement schemes to turbulent flows

Michel Costes, Ilias Petropoulos, Fabien Gand, Paola Cinnella

Association Aéronautique et Astronautique de France

55th 3AF International Conference on Applied Aerodynamics
23 — 25 March 2020, Poitiers – France

FP18-AERO2020-costes

APPLICATION OF HIGH-ORDER VORTICITY CONFINEMENT SCHEMES TO TURBULENT FLOWS

M. Costes[(1)], I. Petropoulos[(2)], F. Gand[(3)] and P. Cinnella[(4)]

[(1)]*ONERA, The French Aerospace Lab, F-92190 Meudon, France, michel.costes@onera.fr*
[(2)]*ONERA, The French Aerospace Lab, F-92190 Meudon, France, ilias.petropoulos@onera.fr*
[(3)]*ONERA, The French Aerospace Lab, F-92190 Meudon, France, fabien.gand@onera.fr*
[(4)]*DynFluid Lab., Arts et Métiers ParisTech, F-75013 Paris, France, paola.cinnella@ensam.eu*

ABSTRACT

This paper presents the application of high-order vorticity confinement (VC) to the simulation of two cases: the decay of compressible homogeneous isotropic turbulence (HIT) in an implicit LES approach and a flat plate with zero pressure gradient in a hybrid RANS/LES simulation. For the HIT case, VC has been found to reduce the numerical dissipation of vortex structures alongside a hybrid low-/high-order baseline scheme. The improvement is mostly identified in the computation of enstrophy and the turbulent kinetic energy spectrum. For the flat plate case, VC has been applied with the mode 3 of ZDES, allowing a better conservation of the turbulent eddies which are injected in the boundary layer with the Synthetic Eddy Method. Small improvements in the log region of the velocity profiles could be noted. A large but contradictory effect on skin-friction and momentum thickness, believed to be due to the source term formulation presently adopted, could also be noted. Globally, the VC methodology does not introduce artificial modifications to the complex vortex dynamics present in turbulent flows.

1. INTRODUCTION

The fast dissipation of vortical structures in CFD solutions is a well-known problem. CFD methods require to be dissipative for stability. As a result, non-physical diffusive terms are introduced in flow regions with large gradients. This does not affect too much shock waves where characteristic lines bring information from the outer flow toward the discontinuity so that a balance between diffusion and physical steepening is reached, depending on the numerical scheme and on the grid fineness. No corresponding balance can be obtained with contact discontinuities and vortices because characteristic lines are tangent to the discontinuity. Consequently, these flow structures are continuously diffused in numerical solutions, at a rate much larger than what would be naturally obtained from the dynamic viscosity of the flow and from turbulent diffusion.

A straightforward approach to minimize this numerical diffusion is to increase the mesh resolution and/or the order of discretization of the numerical scheme. Nevertheless, in both cases the numerical dissipation is still added to the physical diffusion due to turbulence and viscosity. This is why other alternatives have been investigated, among which the Vorticity Confinement method proposed by Steinhoff [25, 26, 27]. Basically, this method consists in adding negative dissipation inside vortical regions of the flow to counter the diffusive effect of the underlying scheme. Over the years, two VC terms have been introduced by Steinhoff, named VC1 and VC2, which have also been investigated at ONERA. VC1 appears to be very efficient, but it is affected by two weaknesses: it is singular at vortex centers and the method cannot be put in conservation form. VC2 does not suffer from these two defects and is therefore better adapted to numerical discretization. However, the original method is first-order accurate only. Therefore it is hardly compatible with higher-order discretizations because the truncation error is dominated by the VC term, and VC2 is worth using with standard second-order discretization schemes only. In order to better adapt the effect of VC and thus increase the accuracy of the simulations, high-order extensions of the VC2 scheme have been developed at ONERA [3, 4, 20].

Up to now the application of VC to turbulent flows has hardly been investigated [14, 21], and as to the authours knowledge, it has never been applied to simulate the large scales of vorticity present in turbulent boundary layers. The purpose of the present work is to investigate the capability of VC to simulate turbulent free-shear and wall-bounded flows properly. As vorticity is inherently present in turbulent flows, the negative dissipation applied to the large number of eddies captured in the flow-field should not distort the flow statistics. This is therefore a demanding type of flows for the method.

2. METHODOLOGY

2.1 Vorticity Confinement

Vorticity Confinement schemes have been introduced by Steinhoff as a source term in the momentum equation:

$$\frac{\partial \rho \vec{v}}{\partial t} + \vec{\nabla} \cdot \left(\rho \vec{v} \otimes \vec{v} + p\bar{\bar{I}} - \bar{\bar{\tau}} \right) = \vec{f}_i \tag{1}$$

Here, we consider only VC2 confinement schemes of increasing order, so that i, the subscript of $\vec{f}$ in Eq. (1) stands for the order of the VC2 scheme. It is necessarily odd as it is an antidissipative term. First-, third- and fifth-order confinement are considered, based on the same vector $\vec{\alpha} = -(\mu\vec{\omega} - \varepsilon\vec{\mathrm{w}})$. First-order VC2 is the original term proposed by Steinhoff. Third- and fifth-order terms are obtained by recursively applying the curl operator to the original term, giving the Laplacian and the bi-Laplacian of first-order VC:

$$\begin{aligned} \vec{f}_1 &= \vec{\nabla} \times \vec{\alpha} \\ \vec{f}_3 &= -\vec{\nabla} \times \left(\vec{\nabla}^2 \vec{\alpha} \right) \\ \vec{f}_5 &= \vec{\nabla} \times \left(\vec{\nabla}^2 \left(\vec{\nabla}^2 \vec{\alpha} \right) \right) \end{aligned} \tag{2}$$

Here, $\vec{\omega}$ is the vorticity vector and $\vec{\mathrm{w}} = \frac{\vec{\omega}}{\omega} \left[\frac{\sum_{l=1}^{N} \omega_l^{-1}}{N} \right]^{-1}$ is the confinement vector, aligned with vorticity and of magnitude equal to the harmonic mean of the vorticity modulus of the surrounding grid points. The confinement parameters μ and ε have to be prescribed by the user. Their role can be understood by taking the curl of Eq. (1) to derive the vorticity transport equation. The first one is a dissipation parameter for improved stability of VC, which should be as small as possible, while the second one is the true anti-dissipative parameter, which should be of the same order of magnitude as the dissipation term of the underlying numerical scheme.

Vorticiy confinement is applied only in regions of the flow where vorticity is detected. Numerically speaking, vorticity does not vanish in irrotational regions, so that a threshold has to be defined below which the flow is considered as irrotational. This threshold value can be based on the standard Q-criterion, or on its normalized version by the symmetric part of the velocity gradient tensor. It was found that this second criterion excludes near-wall regions, which is a desired property for not modifying the modelled part of the boundary layer. However, as the VC term is applied as a source term of the momentum equation, at these detected boundaries the scheme is not rigorously conservative because of the near-wall vorticity. A truly conservative formulation is nevertheless possible by expressing VC2 as a flux-correction term [20, 19], not applied in the present work.

2.2 Numerical Methods and Test Cases

2.2.1 Methods

VC2 schemes were implemented in two solvers of the compressible Navier-Stokes equations using a Finite-Volume approach on structured grids: the DynHoLab research code of the DynFluid laboratory [17] and the elsA industrial code, property of ONERA, Safran and Airbus [2]. In the following, they were applied together with consistent underlying numerical schemes based on high-order MUSCL extrapolation.

In DynHoLab, flux extrapolation is considered, thus the leading truncation error is known. The confinement parameter ε is then set to a value of the same order of magnitude as the truncation error coefficient. The numerical flux is a high-order generalization of the Jameson-Schmidt-Turkel (JST) scheme and at p-th order of accuracy is written:

$$\mathscr{F}_{\mathrm{J}+\frac{1}{2}} = \left(\sum_{\ell=0}^{(p-1)/2} b_\ell \, \delta^{2\ell} \right) \mu \mathrm{F} - \lambda_{\mathrm{J}+\frac{1}{2}} \left[\epsilon^{(2)}_{\mathrm{J}+\frac{1}{2}} \, \delta \overline{W} + \epsilon^{(p+1)}_{\mathrm{J}+\frac{1}{2}} \, \delta^{p} \overline{W} \right]$$

where the coefficients b_ℓ were derived in Ref. [13] and $\lambda_{\mathrm{J}+\frac{1}{2}}$ is an approximation of the spectral radius of the inviscid flux Jacobian matrix on the interface. The average and differencing operators are respectively:

$$\mu(\bullet) = \mu(\bullet)_{\mathrm{J}+\frac{1}{2}} \triangleq \frac{1}{2} \left((\bullet)_{\mathrm{J}+1} + (\bullet)_{\mathrm{J}} \right)$$

$$\delta(\bullet) = \delta(\bullet)_{\mathrm{J}+\frac{1}{2}} \triangleq (\bullet)_{\mathrm{J}+1} - (\bullet)_{\mathrm{J}}$$

The dissipation coefficients at the interface $\mathrm{J}+\frac{1}{2}$ are:

$$\epsilon^{(2)}_{\mathrm{J}+\frac{1}{2}} = k_2 \max\left(\nu_{\mathrm{J}}, \nu_{\mathrm{J}+1}\right)$$

$$\epsilon^{(p+1)}_{\mathrm{J}+\frac{1}{2}} = (-1)^{((p-1)/2)} \max\left(0, k_p - \epsilon^{(2)}_{\mathrm{J}+\frac{1}{2}}\right)$$

where ν_{J} is the JST scheme pressure-based shock sensor. k_p are the baseline artificial dissipation coefficients, which unless otherwise stated are taken $k_2 = 1.0$, and $k_5 = 1/60$ or $k_9 = 1/1260$ respectively at 5th- and 9th-order of accuracy. In some cases, the schemes' pressure-based sensor was multiplied with the Ducros sensor [11],

aiming at reducing the effect of the low-order dissipation within vortices. To better isolate the effect of space discretization, time integration is performed using a 6-stage Runge-Kutta explicit scheme with optimized coefficients [1].
In elsA, a modified version of the AUSM+(P) scheme described by Mary and Sagaut in [15] is used for inviscid flux approximation, while viscous terms use a second-order centered scheme. A sensor to estimate the smoothness of the local solution allows reducing numerical dissipation by discriminating numerical odd-even fluctuations from physical ones. High-order MUSCL extrapolation is performed on the primitive variables so the scheme is formally second-order accurate, albeit its effectively reduced dissipation. In that case the confinement parameters were determined empirically for the simple case of inviscid advection of a well-resolved vortex over long distances. Additionally, a second-order accurate implicit resolution in time is used based on a three-levels backward discretisation of the time derivatives (Gear scheme). At each time step Newton sub-iterations are used together with LU-SSOR decomposition to solve the nonlinear system.

2.2.2 Test cases

The DynHoLab code was applied to compute the decay of isotropic homogeneous turbulence (HIT) in an implicit LES approach (i.e. without subgrid scale modeling). This approach is specifically appropriate for the finer evaluation of the schemes' numerical dissipation. The problem is solved on a periodic box of dimensions $[0,2\pi]^3$ discretized by an 128^3-cell Cartesian grid. The employed initialization results in a divergence-free velocity field without fluctuations of thermodynamic quantities. The flow field thus displays a rapid initial stage during which dilatational fluctuations, velocity correlations and thermodynamic fluctuations are developed. Initial velocity fluctuations are assumed to follow a prescribed spectrum of the form $\mathrm{E}(\kappa) = A_0\,\kappa^4 \exp\left(-2\,\kappa^2/{\kappa_0}^2\right)$, where κ_0 is the wavenumber corresponding to the energy spectrum peak and A_0 is a real coefficient that determines the initial volume averaged kinetic energy K_0. The initialization method has been thoroughly validated in Ref. [24]. Simulations were performed at $Re_\lambda = 175$ based on the Taylor microscale, with the spectrum peak fixed at $\kappa_0 = 4$. The initial condition corresponds to an initial turbulent Mach number $M_{t0} = \langle u'^2 + v'^2 + w'^2\rangle^{1/2}/\langle a\rangle = 1.0$, with $\langle a\rangle$ being the volume average of the speed of sound. Conditions corresponding to such high turbulent velocity fluctuations result in the formation of eddy shocklets during the main part of the HIT decay [22]. The objective of high-order VC in this case is the balancing of the high-order part of the baseline numerical dissipation within vortices. At the same time, the low-order part of the baseline numerical dissipation should remain minimally affected as it is required for the damping of numerical oscillations in the vicinity of shocks.
The flat-plate case is the one proposed by ONERA for the EU Go4Hybrid project [7]. It was also considered by Deck et al. in [10], and these results will be used in the following as reference, together with experimental results from De Graaf et al. [5] and DNS results from Schlatter et al. [23]. It concerns a zero-pressure gradient turbulent boundary layer over a flat plate, with a freestream velocity of 70 m/s, a freestream static pressure and temperature of 99120 Pa and 287 K respectively, so that the Reynolds number equals Re=4.72 10^6 per unit length (meter). Initial conditions correspond to a boundary layer thickness $\delta_0 = 5.8$ mm and the corresponding inlet boundary layer profiles were prescribed as suggested in [7]. It was computed with elsA on the same mesh as Deck's one, which has 7.8 Millions points, using the mode 3 of the ZDES method [6, 8]. In this Wall-Modelled LES version of ZDES, the external part of the boundary layer is considered in LES down to the logarithmic region (0.125 δ_0 in our case), the near wall part being described in RANS mode. The method thus requires the generation of turbulence at the inlet in the LES part of the boundary layer. The Synthetic Eddy Method (SEM) introduced by Jarrin et al. [12], improved by Pamiès et al. [18] and adapted to ZDES by Deck et al. in [9], was used for that purpose.

3. RESULTS

3.1 Compressible Homogeneous Isotropic Turbulence

The compressible HIT case is computed up to a final time $10\,\tau_e$, where τ_e is the large-eddy turnover time. Computations with VC are performed at 5th-order of accuracy, and compared against the baseline 5th-order scheme. The non-dimensional values of the confinement parameters in this case are $\mu = 0$ and $\varepsilon = 1.2\,k_5$. A broader exploration of the effect of different parameters is presented in Ref. [19, 21] at lower initial turbulent Mach number conditions. Computations performed with a 9th-order accurate scheme are used as a reference.
The evolution of enstrophy is shown in Fig. 2. The computed peak enstrophy value is used as a measure of the schemes' resolution. Schemes without the Ducros sensor are shown to have very similar resolvability in this case. This is due to the strong compressible effects causing the schemes' accuracy to be dominated by the low-order part of the dissipation, which is the same for all schemes. Still, the 5th-order scheme with VC gives a solution closer to the 9th-order reference than its baseline version. The use of the Ducros sensor limits the effect of the low-order dissipation within vortices, thus revealing the effect of the schemes' different high-order dissipation on the resolution of vortical structures. Due to

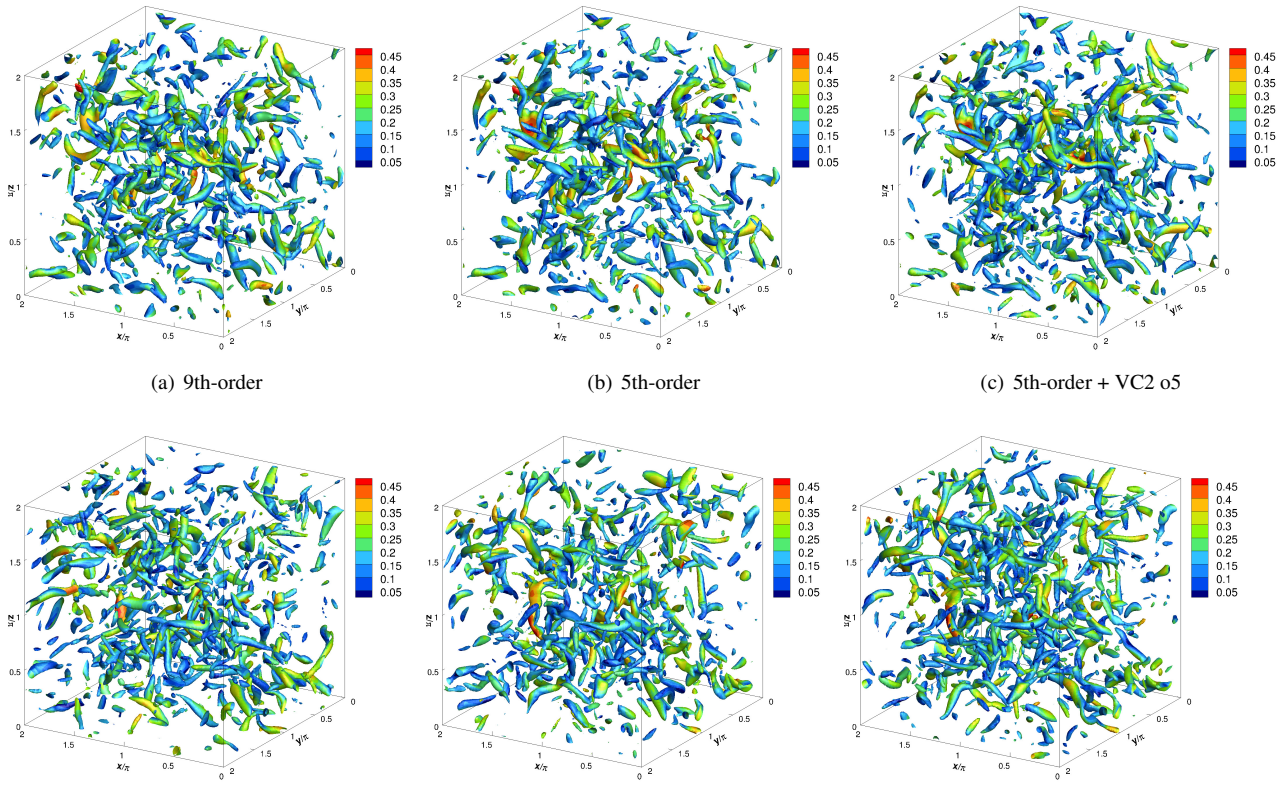

(a) 9th-order (b) 5th-order (c) 5th-order + VC2 o5

(d) 9th-order (Ducros, $k_9 = 1/630$) (e) 5th-order (Ducros) (f) 5th-order (Ducros) + VC2 o5

Figure 1: Instantaneous view of an iso-surface of the Q criterion colored by the local Mach number at $t = 10\tau_e$. Compressible HIT case at $M_{t0} = 1.0$.

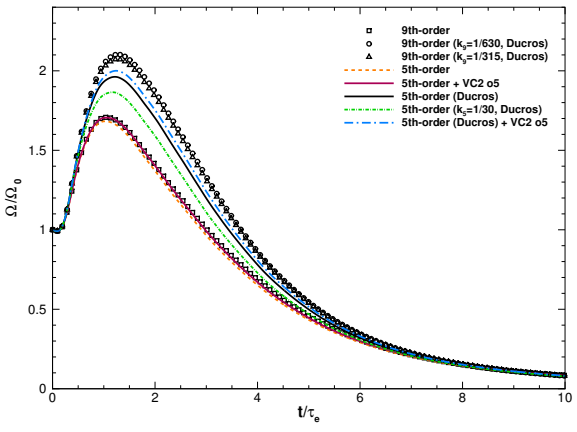

Figure 2: Time evolution of enstrophy at $M_{t0} = 1.0$ for different numerical numerical schemes.

the low dissipation of the baseline 9th-order scheme, applying the Ducros sensor required to increase the value of the high-order artificial-dissipation coefficient to stabilize the scheme. Increasing the baseline artificial dissipation coefficient naturally has a noticeable effect on the resolvability of the scheme, particularly at 5th-order of accuracy. The use of VC is again shown to give a solution closer to the 9th-order reference than the baseline 5th-order version. A qualitative representation with respect to the preservation of vortical structures is shown in Fig. 1 at time $t = 10\tau_e$. Results overall do not show significant differences between the different schemes. An improvement in the preservation of turbulent structures can however be noted with the introduction of VC, both with and without the Ducros sensor.

A finer investigation of the schemes' resolvability can be made through the turbulent kinetic energy spectra, shown in Fig. 3. At $t = 2\tau_e$, closer to the time of the enstrophy peak, the effect of the Ducros sensor is apparent in a large part of the energy spectrum. The effect of VC is positive but relatively smaller in comparison to that of the baseline artificial dissipation coefficient, an increase of which results in a noticeable reduction of the cut-off wavenumber both at 5th- and 9th-order of accuracy. Moreover, the 9th-order scheme ($k_9 = 1/1260$) without the Ducros sensor shows an increase of small-scale kinetic energy. This is a result of its lower dissipation, an effect which is balanced over time. At $t = 10\tau_e$, numerical scheme effects are localized in the higher frequency part of the spectrum. At this later stage of the decay

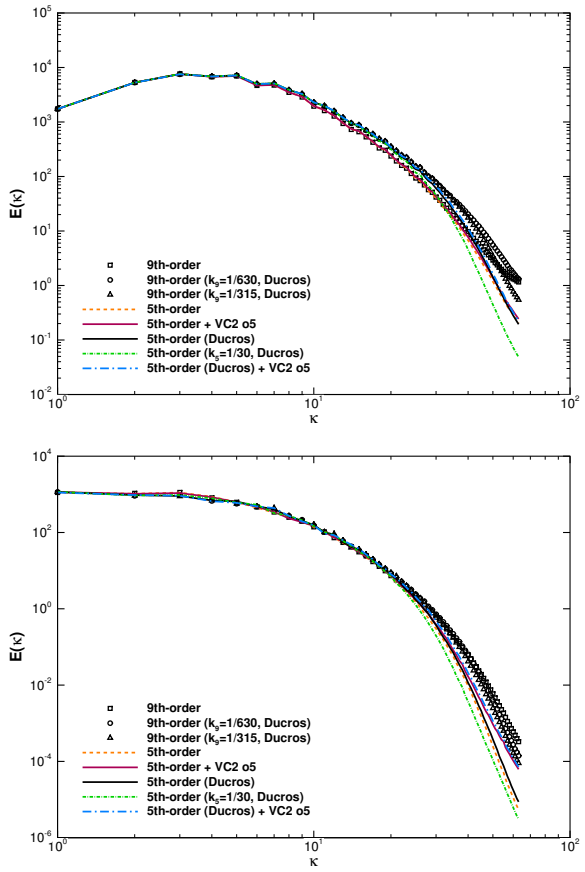

Figure 3: Turbulent kinetic energy spectrum for the compressible HIT case at $M_{t0} = 1.0$. Time $t = 2\,\tau_e$ (top) and $t = 10\,\tau_e$ (bottom).

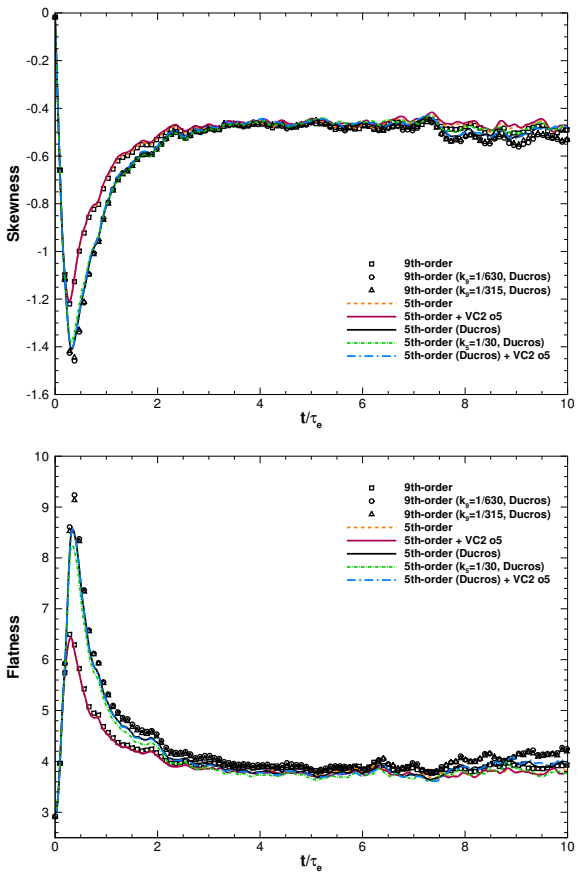

Figure 4: Skewness and flatness factor of the fluctuating velocity gradient distribution for the compressible HIT case at $M_{t0} = 1.0$.

phase, where viscous effects become dominant and accumulated over time, the effect of the Ducros sensor is shown to be smaller compared to the differences in the high-order dissipation terms. Schemes with VC show better resolvability than their baseline version, extending the dissipation cut-off of the energy spectrum. Fig. 4 shows the evolution of high-order statistical moments of the fluctuating velocity gradient distribution, which can be sensitive to the space discretization scheme. The effect of the Ducros sensor is notable at the early stages of the flow. VC is shown to provide results consistent with the baseline schemes, without any negative influence on the statistical moments.

Overall, the Ducros sensor was found to be capable of reducing the dominant effect of the low-order part of the baseline dissipation due to the strong compressibility effects. An increase of the baseline artificial dissipation coefficients naturally has a rather important influence on the schemes' resolvability. At the same time, VC is shown to improve the preservation of vortical structures without any noticeable negative counterpart to the turbulent flow dynamics. Last, the compatibility of VC with the Ducros sensor in this compressible case is interesting and demonstrates that the stable effect of the non-linear anti-dissipation of VC is not a result of a stabilizing effect of the baseline low-order dissipation. Both numerical strategies aim at separately balancing the effect of the baseline numerical dissipation within vortices, its low-order part being balanced by the Ducros sensor and its high-order part being balanced by the high-order VC term.

3.2 Zero Pressure Gradient Flat Plate

For these simulations, the time step used corresponds to $\Delta t\ U_\infty/L = 3.4\ 10^{-5}$ in convective time units, based on free-stream velocity U_∞ and flat plate length L, and 4 Newton sub-iterations were applied at each time step. In each case, the solution was initialized with the same RANS solution and run over a convective time of about 3.4 units to remove transient effect, then flow statistics were recorded over 4.3 additional convective time units without VC and 5.1 convective time units with VC.

The effect of VC on wall-resolved turbulence is plotted at a similar time of the simulation for all cases in Fig. 5, Fig.

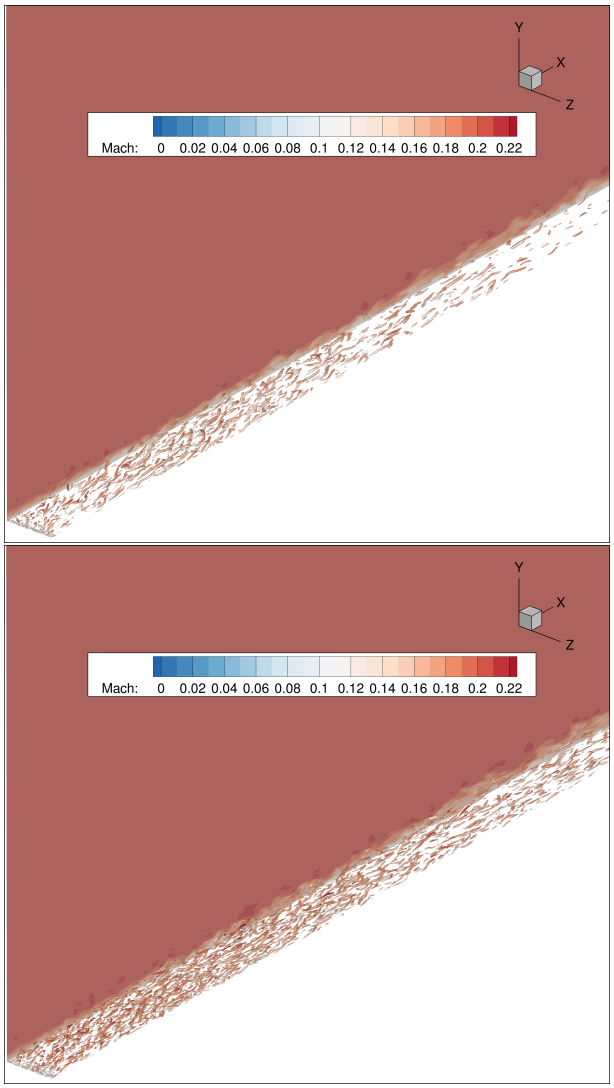

Figure 5: Instantaneous view of $Q = 1/4\,(U_\infty/\delta_0)$ criterion coloured by Mach number for baseline case (top), first-order VC2 (bottom).

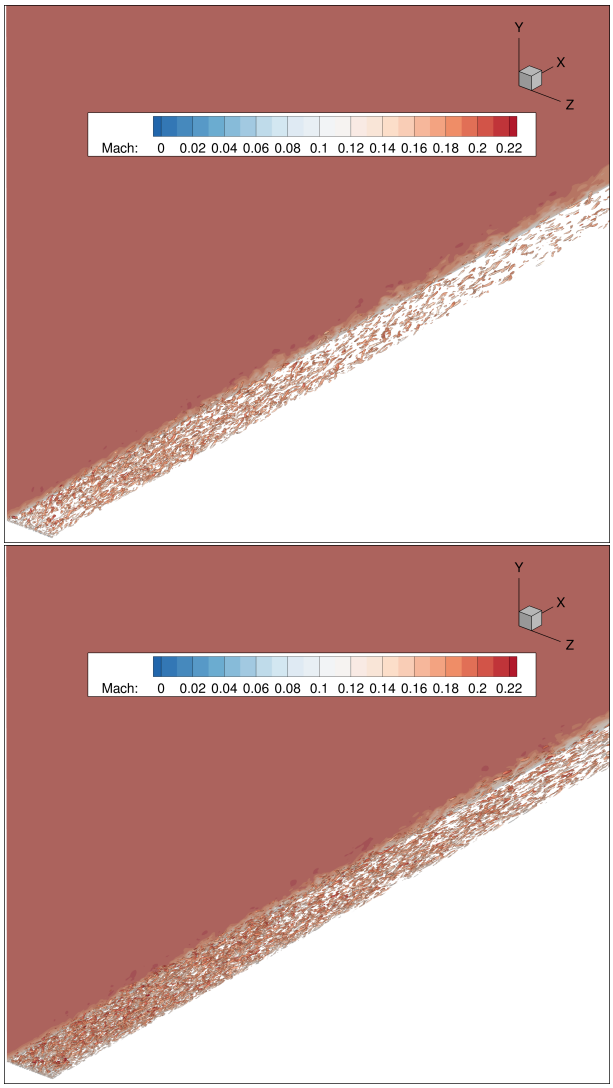

Figure 6: Instantaneous view of $Q = 1/4\,(U_\infty/\delta_0)$ criterion coloured by Mach number for baseline case (top), third-order VC2 (bottom).

6 and Fig. 7 for 1^{st}, 3^{rd} and 5^{th}-order VC respectively. Without confinement, the turbulent content of the boundary layer is improved with the order of extrapolation of the MUSCL scheme, thus showing that the corresponding numerical dissipation is being reduced correspondingly. Furthermore, at each nominal order of the scheme, VC yields a significantly richer content in terms of turbulent eddies with respect to its baseline counterpart, even in the donwstream region where the mesh resolution is relaxed in order to prevent wave reflections at the outlet.
The effect of confinement on time-averaged velocity profiles is presented in Fig. 8 at a chordwise station $x/\delta_0 = 40$ where the simulated boundary layer has relaxed towards a fully turbulent one. The results obtained by Deck in [10], DNS results from Schlatter et al. [23] and experimental results from De Graaf et al. [5], both for momentum thickness Reynolds numbers in a similar range, are also plotted for comparison. The effect of VC is small, but the evolution in the log region is generally improved, more especially at 3^{rd}-order, providing results slightly closer to reference data, either from DNS or from experiment.
Nevertheless, such a difference may be partly due to the effect of VC on skin-friction, shown in Fig. 9, as the friction velocity u_τ used for normalization is directly related to skin-friction. At 1^{st}-order, the skin-friction coefficient along the flat plate is increased, deviation of results without and with VC starting 5 δ_0 after the inlet and showing increasing differences down to more than 20 δ_0 where the confined solution starts to relax towards the classical flat-plate solution. On the contrary, the baseline computation requires more than twice this distance to approach

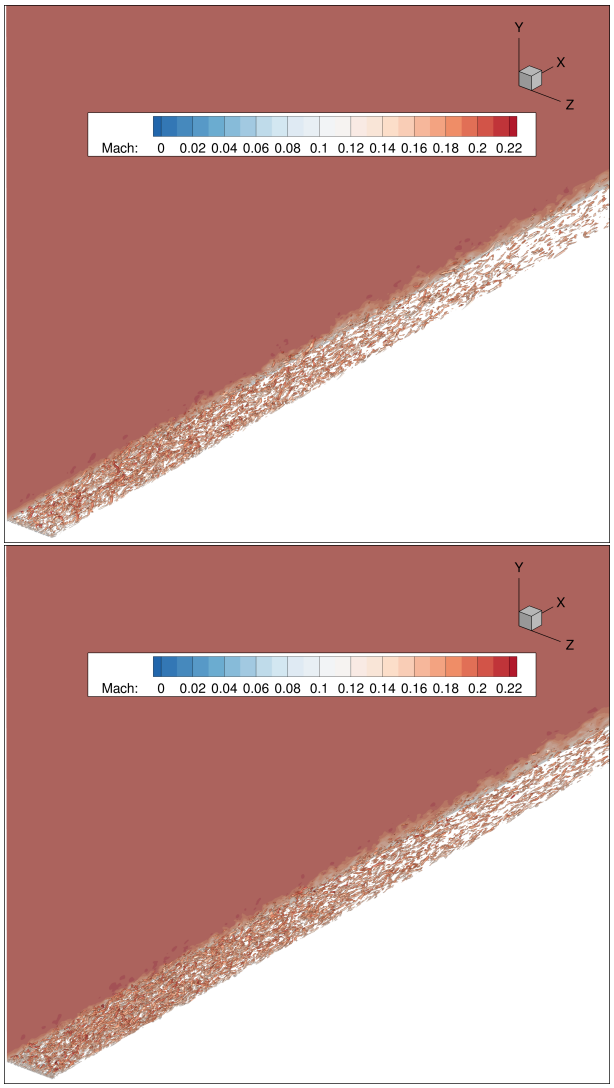

Figure 7: Instantaneous view of $Q = 1/4\,(U_\infty/\delta_0)$ criterion coloured by Mach number for baseline case (top), fifth-order VC2 (bottom).

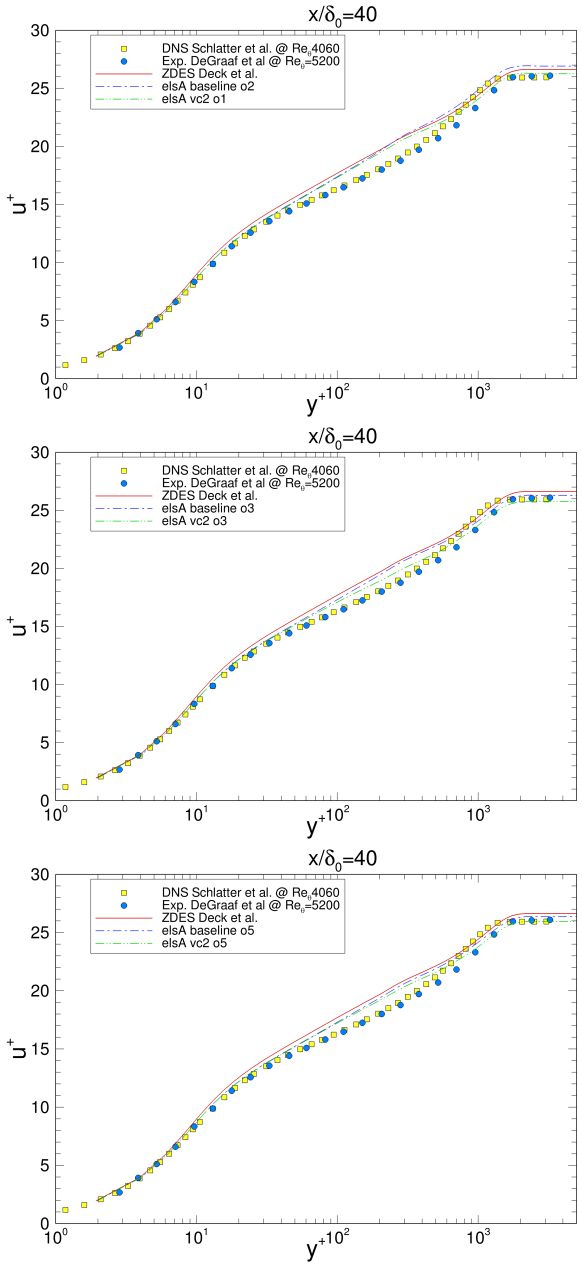

Figure 8: Effect of vorticity confinement on velocity profile at $x/\delta_0 = 40$ for first- (top), third- (middle) and fifth-order VC2 (bottom).

the true solution, thus resulting in a streamwise gradient of skin-friction larger (i.e. less negative) than predicted by the confined solution. Reference results, either from experiment [5], [16] or from DNS [23], as well as the analytical Coles-Fernholz correlation are included for comparison. Additionally, the results of Deck et al [10], obtained with 3^{rd}-order MUSCL extrapolation, are also plotted, showing that the effect of 1^{st}-order VC is to bring the underlying 2^{nd}-order solution very close to the standard 3^{rd}-order one. At 3^{rd}-order, the skin-friction computed with VC converges faster to the turbulent boundary layer reference data than the baseline simulation too, although the effect is much smaller than at 1^{st}-order. However, friction values obtained with VC then become too high, at the limit of the +5% tolerance above the Coles-Fernholz analytical curve while the baseline computation seems to be fairly correct in predicting this parameter. A similar effect is also obtained at 5^{th}-order, though with a smaller difference between confined and baseline predictions. Both solutions are inside the 5% tolerance interval around the Cole-Fernholz formula. Furthermore, the skin-friction predicted at 5^{th}-order with and without VC converge towards the theoretical curve earlier than the 3^{rd}-order results obtained by Deck.

The evolution of momentum thickness for all cases is plotted in Fig. 10. Considering the integral momentum

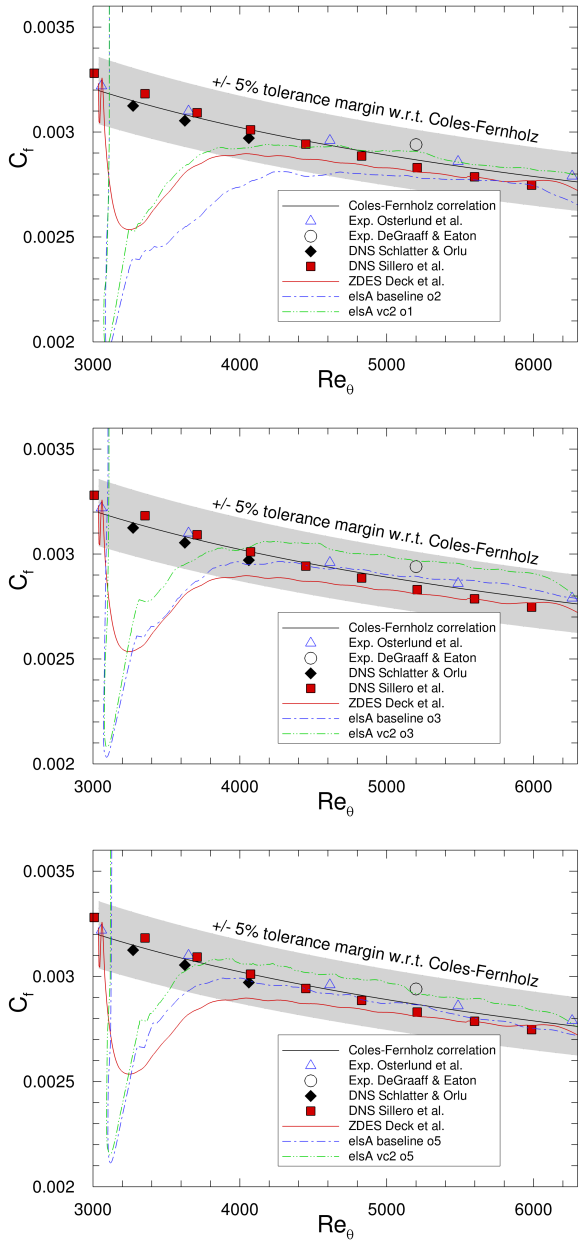

Figure 9: Effect of vorticity confinement on skin-friction for first- (top), third- (middle) and fifth-order VC2 (bottom).

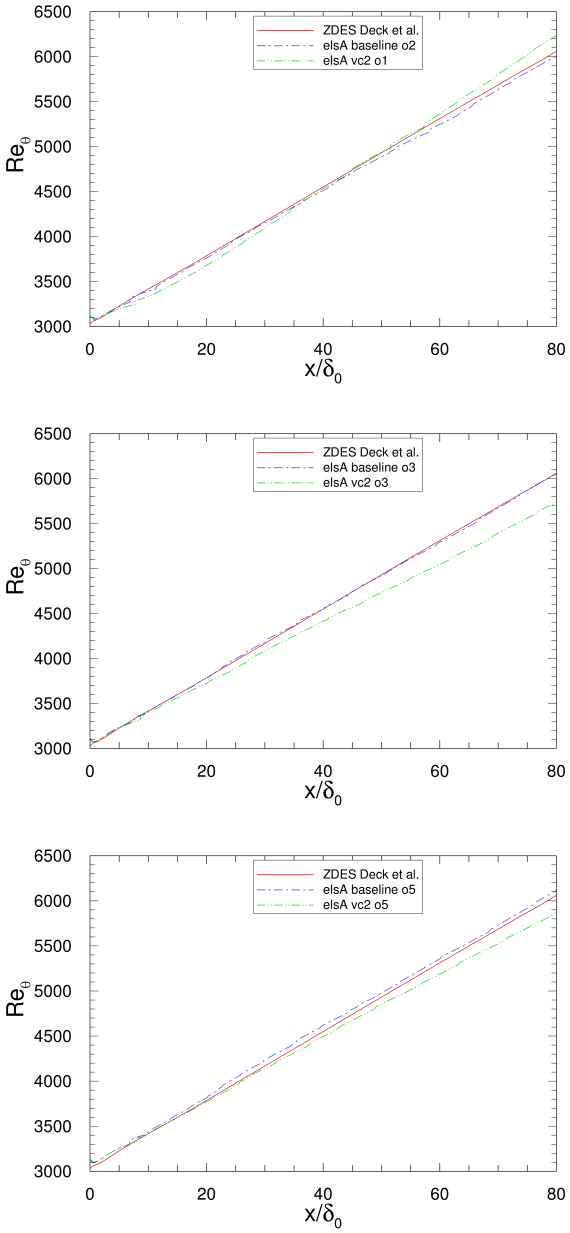

Figure 10: Effect of vorticity confinement on momentum thickness for first- (top), third- (middle) and fifth-order VC2 (bottom).

equation (3):

$$\frac{d\theta}{dx} = \frac{C_f}{2} \tag{3}$$

this parameter should closely follow the evolution of skin-friction. However, this is not the case when VC is activated, especially at 3^{rd}- and 5^{th}-order, since the momentum thickness computed with VC is found to have a smaller streamwise gradient than without VC, while higher skin-friction values are obtained. It is likely that this inconsistency is due to the non-conservativity of the source term approach of VC presently used. The formulation is actually conservative in the inner domain where VC is applied because the source term is in curl form, but there may occur errors at the boundaries if vorticity cannot be neglected there. This is more particularly the case in the near-wall region which is removed from confinement, as desired, but where local vorticity is actually found. This can be corrected by expressing VC as a flux correction (e.g. applying $\vec{S} \times \vec{\alpha}$ at the cell faces instead of $\Omega \vec{\nabla} \times \vec{\alpha}$ at the cell center). Such a modification will

be tested in the near future to check that the present argument is correct.

4. CONCLUSIONS

The present work showed the evaluation of vorticity confinement schemes of order 1, 3 and 5 to the simulation of turbulent flows.
In the compressible HIT case, VC was applied alongside schemes with hybrid low-/high-order numerical dissipation. The scheme with VC was found to have better resolvability than its baseline version, giving results closer to the reference 9th-order computations. At the same time, it was shown to be compatible with the use of the Ducros sensor.
In the flat plate case, VC allows a better conservation of the turbulent eddies which are injected in the BL with the Synthetic Eddy Method. Application of VC also brings a small improvement in the log region of the velocity profiles. It also has a large but contradictory effect on skin-friction and momentum thickness. This is believed to be due to the source term formulation presently adopted, which introduces conservation errors in the near-wall region of the BL at the boundary where VC is deliberately excluded from confinement. This can be corrected by adopting a new flux-correction form of VC.
Globally, the results obtained in this work show that, besides ensuring the computation of vorticity with reduced dissipation, the VC methodology does not introduce artificial modifications to the complex vortex dynamics present in turbulent flows and boundary layers, which is an important property of the method.

REFERENCES

[1] C. Bogey and C. Bailly. A family of low dispersive and low dissipative explicit schemes for flow and noise computations. *Journal of Computational Physics*, 194(1):194–214, 2004.

[2] L. Cambier, S. Heib, and S. Plot. The Onera elsA CFD software: input from research and feedback from industry. *Mechanics & Industry*, 14(3):159–174, 2013.

[3] M. Costes and F. Juillet. Analysis and higher-order extension of the VC2 confinement scheme. *Computers & Fluids*, 56(0):102 – 117, 2012.

[4] M. Costes, I. Petropoulos, and P. Cinnella. Development of a third-order accurate vorticity confinement scheme. *Computers & Fluids*, 136:132–151, 2016.

[5] D. B. De Graaff and J. K. Eaton. Reynolds-number scaling of the flat-plate turbulent boundary layer. *Journal of Fluid Mechanics*, 422:319–346, 2000.

[6] S. Deck. Recent improvements in the zonal detached eddy simulation (ZDES) formulation. *Theoretical and Computational Fluid Dynamics*, 26(6):523–550, 2012.

[7] S. Deck. The spatially developing flat plate turbulent boundary layer. In *Go4Hybrid: Grey Area Mitigation for Hybrid RANS-LES Methods*, pages 109–121. Springer, 2018.

[8] S. Deck, N. Renard, R. Laraufie, and P. Sagaut. Zonal detached eddy simulation (ZDES) of a spatially developing flat plate turbulent boundary layer over the Reynolds number range 3 150 $\leq$ Re $\theta \leq$ 14 000. *Physics of Fluids*, 26(2):025116, 2014.

[9] S. Deck, P.-E. Weiss, M. Pamiès, and E. Garnier. Zonal detached eddy simulation of a spatially developing flat plate turbulent boundary layer. *Computers & Fluids*, 48(1):1–15, 2011.

[10] S. Deck, P.-E. Weiss, and N. Renard. A rapid and low noise switch from RANS to WMLES on curvilinear grids with compressible flow solvers. *Journal of Computational Physics*, 363:231–255, 2018.

[11] F. Ducros, V. Ferrand, F. Nicoud, C. Weber, D. Darracq, C. Gacherieu, and T. Poinsot. Large-eddy simulation of the shock/turbulence interaction. *Journal of Computational Physics*, 152(2):517–549, 1999.

[12] N. Jarrin, S. Benhamadouche, D. Laurence, and R. Prosser. A Synthetic-Eddy-Method for Generating Inflow Conditions for Large-Eddy Simulations. *International Journal of Heat and Fluid Flow*, 27:585–593, 2006.

[13] A. Lerat and C. Corre. *High-order residual-based compact schemes on structured grids*. von Karman Lecture Series 2006-01. von Karman Institute for Fluid Dynamics, November 2005.

[14] N. Lynn and J. Steinhoff. Large reynolds number turbulence modeling with vorticity confinement. In *18th AIAA Computational Fluid Dynamics Conference*, page 3965, 2007.

[15] I. Mary and P. Sagaut. Large eddy simulation of flow around an airfoil near stall. *AIAA journal*, 40(6):1139–1145, 2002.

[16] J. M. Österlund, A. V. Johansson, H. M. Nagib, and M. H. Hites. A note on the overlap region in turbulent boundary layers. *Physics of Fluids*, 12(1):1–4, 2000.

[17] P.-Y. Outtier, C. Content, P. Cinnella, and B. Michel. The high-order dynamic computational laboratory for cfd research and applications. In *21st AIAA Computational Fluid Dynamics Conference*, page 2439, 2013.

[18] M. Pamiès, P.-E. Weiss, E. Garnier, S. Deck, and P. Sagaut. Generation of Synthetic Turbulent Inflow Data for Large Eddy Simulation of Spatially Evolving Wall-Bounded Flows. *Physics of Fluids*, 21(4):045103–15, 2009.

[19] I. Petropoulos. *Study of high-order vorticity confinement schemes*. PhD thesis, Arts et Métiers ParisTech, 2018.

[20] I. Petropoulos, M. Costes, and P. Cinnella. Development and analysis of high-order vorticity confinement schemes. *Computers & Fluids*, 156:602–620, 2017.

[21] I. Petropoulos, M. Costes, and P. Cinnella. Vortical flow calculations using a high-order vorticity confinement method. In *23rd AIAA Computational Fluid Dynamics Conference*, page 3291, 2017.

[22] R. Samtaney, D. I. Pullin, and B. Kosović. Direct numerical simulation of decaying compressible turbulence and shocklet statistics. *Physics of Fluids*, 13(5):1415–1430, 2001.

[23] P. Schlatter and R. Örlü. Assessment of direct numerical simulation data of turbulent boundary layers. *Journal of Fluid Mechanics*, 659:116–126, 2010.

[24] L. Sciacovelli. *Numerical simulation of dense gas turbulent flows*. PhD thesis, Arts et Métiers ParisTech, 2016.

[25] J. Steinhoff and N. Lynn. *Treatment of vortical flows using vorticity confinement*. Chapter 10 of Computing the Future IV: Frontiers of Computational Fluid Dynamics. Springer-Verlag, 2006.

[26] J. Steinhoff, N. Lynn, and L. Wang. *Large eddy simulation using vorticity confinement*. Chapter 4 of Implicit Large Eddy Simulations: Computing Turbulent Flow Dynamics. Cambridge University Press, 2006.

[27] J. Steinhoff, N. Lynn, W. Yonghu, M. Fan, L. Wang, and W. Dietz. *Turbulent flow simulations using vorticity confinement*. Chapter 12 of Implicit Large Eddy Simulations: Computing Turbulent Flow Dynamics. Cambridge University Press, 2006.